Equid que venihi tasped volut officillum sidit lam p. XX

Quasi volut accae cullit and queomni quis pp. XX & XX

Perspedi cuptatur audicto volut accae cullit p. XX

Science

$15
7 AUGUST 2020
sciencemag.org

AAAS

BUBBLE RUPTURE

Surface tension drives the wrinkling and collapse in viscous fluids p. XXX

FLUID MECHANICS

A new wrinkle on liquid sheets: Turning the mechanism of viscous bubble collapse upside down

Alexandros T. Oratis[1], John W. M. Bush[2], Howard A. Stone[3], James C. Bird[1]*

Viscous bubbles are prevalent in both natural and industrial settings. Their rupture and collapse may be accompanied by features typically associated with elastic sheets, including the development of radial wrinkles. Previous investigators concluded that the film weight is responsible for both the film collapse and wrinkling instability. Conversely, we show here experimentally that gravity plays a negligible role: The same collapse and wrinkling arise independently of the bubble's orientation. We found that surface tension drives the collapse and initiates a dynamic buckling instability. Because the film weight is irrelevant, our results suggest that wrinkling may likewise accompany the breakup of relatively small-scale, curved viscous and viscoelastic films, including those in the respiratory tract responsible for aerosol production from exhalation events.

Wrinkling of thin sheets appears in a variety of settings across a wide range of length scales, including those in neutrophil phagocytosis (*1*), in the development of the epithelial tissue responsible for fingerprints (*2*), and in subduction zones in plate tectonics (*3*). Generally speaking, sheets wrinkle because they require less energy to buckle than to compress when they are subjected to compressive stresses (*4*). Most recent studies have focused on understanding the bending deformations that occur when a thin elastic sheet is stretched (*5*, *6*), poked (*7*, *8*), or wrapped around a curved object (*9*, *10*); however, viscous liquids can also buckle (*11*–*13*). A visually prominent example is the "parachute instability" that develops spontaneously when a bubble rising in a viscous liquid reaches the surface and ruptures (Fig. 1). Bubbles collect at the surface of viscous liquids during processes including glass manufacturing, spray painting (*14*), vitrification of radioactive waste (*15*), and volcanic eruptions (*16*). Having surfaced, the bubble consists of a thin liquid film in the form of a spherical cap that is supported by the gas trapped inside it (Fig. 1A). When the bubble ruptures, the liquid film develops a growing hole that allows the trapped gas to escape. Without the support of this gas, the forces on the liquid film are unbalanced, causing bubble collapse and the development of radial wrinkles around the bubble periphery. Previous investigations have concluded that the wrinkles develop as a consequence of the weight of the collapsing thin film and the geometric constraint imposed by the opening hole (*17*, *18*). We demonstrate here that the wrinkling instability relies on neither gravity nor the presence of the hole.

The development of wrinkles from a collapsing bubble with radius R = 1 cm on a silicone oil bath with viscosity $\mu \approx 10^6$ cP is illustrated in Fig. 1B. The wrinkles emerged in an isolated annular region near the bubble's edge, when the bubble height Z reached a distance of approximately $Z/R \approx 0.6$ from the bath's surface. Before hole formation, the equilibrium shape of a bubble at the air–liquid interface is established by the balance between the pressure excess inside the bubble, ΔP, and a combination of gravitational and capillary forces (*19*). Because the bubble radius in this example is much larger than the capillary length $(\gamma/\rho g)^{1/2} \approx 1$ mm, where γ is the surface tension, ρ the liquid density, and g the acceleration due to gravity, the bubble extends substantially beyond the bath surface and forms a hemisphere. Gravity drives drainage in the thin hemispherical film, causing the bubble walls to thicken toward the base (*17*). Puncturing the film generates a hole and prompts the film retraction from the point of rupture, driven by surface tension and the local curvature of the hole's rim (*20*–*22*). In addition, puncturing the film equilibrates the pressure across the interface, causing $\Delta P \rightarrow 0$. The presence of the hole thus leaves the capillary and gravitational forces acting on the film unbalanced, ultimately causing the bubble collapse. Considering a surface element dA on the spherical cap, the gravitational force acting on the film thickness h scales as $F_g \sim \rho h g dA$, whereas the capillary force pulling the film inward scales as $F_c \sim (4\gamma/R)dA$ (Fig. 1A). For a centimeter-sized bubble with a characteristic thickness of $h \approx 10$ μm, capillary forces (F_c) dominate gravitational forces (F_g) by a factor of $F_c/F_g \sim 4\gamma/(\rho g R h) \approx 80$. This scaling argument indicates that the collapse process is dominated by surface tension rather than gravity.

To test this hypothesis, we conducted an identical experiment after turning the bubble upside down (Fig. 1C). The approach is possible because the liquid is sufficiently viscous that the experiments can be conducted before the silicone oil flows out of the inverted container. We first prepared the bubble right-side up, and then we rapidly rotated the sample and ruptured the bubble within seconds. When inverted, the bubble film (thickness $h \approx 2.4$ μm) maintained its shape and thickened at the

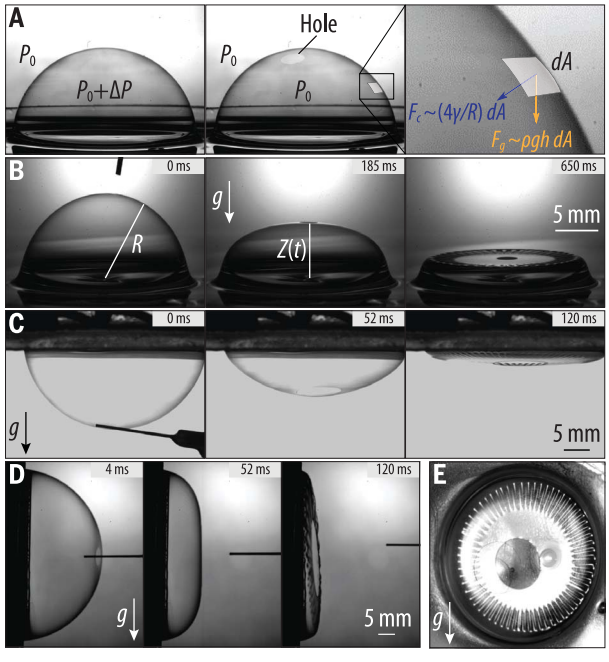

Fig. 1. Collapse of a viscous bubble film upon rupture. (**A**) If a hole develops in the surface of a bubble resting on a liquid surface, then the pressurized air escapes, leaving the gravitational and surface tension forces unbalanced. (**B**) An air bubble with radius R = 1 cm at the surface of a viscous silicone oil bath collapses and its height $Z(t)$ decreases after rupture. As the bubble collapses, wrinkles appear along its periphery. (**C**) When the bubble is rapidly turned upside down and ruptured, it collapses in a similar fashion. (**D** and **E**) Rotating the sample such that its base is parallel to the direction of gravity g results in a similar collapse (D) and wrinkles still appear (E).

[1]Department of Mechanical Engineering, Boston University, Boston, MA 02215, USA. [2]Department of Applied Mathematics, Massachusetts Institute of Technology, Cambridge, MA 02139, USA. [3]Department of Mechanical and Aerospace Engineering, Princeton University, Princeton, NJ 08544, USA.
*Corresponding author. Email: jbird@bu.edu

Downloaded from http://science.sciencemag.org/ on August 6, 2020

apex at a rate of ~10 nm/s; therefore, the film geometry does not vary appreciably during either the rotation or inversion (*23*). If gravity and viscosity were the dominant forces, then the inverted bubble would elongate downward, as previously demonstrated in simulations (*24*). Instead, the inverted bubble retracted upward against the force of gravity, and wrinkles formed again during the final stages of bubble collapse (Fig. 1C). The direction of motion clearly demonstrates that gravity does not drive the collapse; however, it does not rule out the possibility that it is involved in the wrinkles. By repeating the experiment with the bubble on its side (Fig. 1D), we found that wrinkles still appeared (Fig. 1E). We thus conclude that gravity plays a negligible role during bubble collapse and wrinkling instability.

To understand the extent to which surface tension drives bubble collapse, we measured the maximum distance of the bubble film $Z(t)$ from the bath surface. From the evolution of the bubble height with time, we can extract a collapse speed $V = dZ/dt$ that will dictate the characteristic time scale of collapse. If surface tension drives the collapse, then it would be expected that the speed would depend on the competing capillary and viscous forces. Indeed, balancing the capillary force γR with the viscous force $\mu h_0 V$ yields a characteristic velocity $V \sim \gamma R/\mu h_0$, where h_0 is the initial film thickness at the apex (*23*). Therefore, we expect the evolution of the bubble height Z and the associated collapse speed V to depend on both the viscosity and thickness of the film. We tested this conjecture through systematic experiments in which we used silicone oils with viscosities of 100, 800, and 3000 Pa • s and also varied the thickness of the film at rupture. Once punctured, the bubble collapsed, decelerating as it reached the bath surface (Fig. 2A). From the high-speed images, we calculated a representative velocity V at the onset of wrinkling by averaging the downward speed dZ/dt over the range $0.6 < Z/R < 1$ (*23*). Increasing the viscosity of the silicone oil slowed down the collapse. As expected, the data collapse when the normalized height Z/R is plotted against the dimensionless time Vt/R (Fig. 2A, inset).

To gain further insight, we determined the rupture thickness at the bubble apex, h_0, by combining optical techniques with the gravitational drainage theory of Debrégeas *et al.* (*17*). Under a monochromatic light, concentric interference fringes could be seen to emanate from the bubble's apex (Fig. 2B, inset). The circles are evidence of axisymmetric drainage, and the rate at which they appear can be measured with thin-film interferometry to estimate the thickness at the apex (*23*). Thinner bubbles collapsed faster (Fig. 2B), as expected from the predicted scaling $V \sim \gamma R/\mu h_0$ (solid line). We acknowledge sizable deviations of the experimental data from this simple scaling, especially for the 100 Pa • s silicone oil bubbles. Nevertheless, the overall trends support the hypothesis that the bubble collapse is driven by surface tension, in which case the characteristic time scale $R/V \sim \mu h_0/\gamma$ becomes independent of the bubble radius.

The model of da Silveira *et al.* (*18*) suggests that gravity and viscosity lead to wrinkling in such a way that the number of wrinkles scales as $n \sim (\rho g R_H^3 \tau_c/\mu h^2)^{1/2}$, with R_H being the radius of the hole and τ_c the time it takes for the film to collapse. The radius of the hole grows rapidly at early times but slows down sufficiently to be adequately modeled as a constant during the instability. This model thus claims that the number of wrinkles depends strongly on the size of the hole, with no wrinkles predicted if $R_H = 0$. To investigate the role of the hole in the development of wrinkles, we performed experiments by drilling a small opening at the bottom of the petri dish in which the silicone oil was placed. We inserted a narrow tube into the opening, injected air to create the bubble, and then sealed the opening with a valve. Once the bubble had reached the surface to create a hemispherical dome, we opened the valve to allow the pressurized air inside the bubble to escape. When the air escaped, $\Delta P \rightarrow 0$, causing the capillary force from the curved surface to be unbalanced and the bubble to collapse (Fig. 3A). Wrinkles again appeared at the final stages of the collapse, indicating that the hole plays a role in wrinkling only by eliminating the pressure difference across the bubble surface (Fig. 3B). We thus need to revisit the wrinkling dynamics to deduce a consistent physical picture for the wrinkling mechanism.

We propose a mechanism in which the wrinkles result when the crushing dynamics of the spherical film lead to a hoop compression that overcomes the smoothing effects of surface tension. Here, the capillary-driven collapse induces a radial velocity in a cylindrical reference frame that scales as $V_r \sim V \sim \gamma R/\mu h_0$ (Fig. 3A). This radial velocity leads to compression rates $\dot{\varepsilon}_{rr}$ and $\dot{\varepsilon}_{\theta\theta}$ in the radial and azimuthal directions, respectively, for the r,θ coordinate system defined in Fig. 3C. For a Newtonian fluid, this compression generates both a radial stress $\bar{\sigma}_{rr}$ and hoop stress $\bar{\sigma}_{\theta\theta}$, which can be related to the rate of radial compression through a Trouton model (*25*), yielding $\bar{\sigma}_{rr} \sim \bar{\sigma}_{\theta\theta} \sim 4\mu h V_r/R$ for a film with thickness h. Here, the overbar denotes that the 3D stress has been integrated over the thickness, leading to a 2D stress with dimensions of force per length. It follows from our scaling for V_r that $\bar{\sigma}_{rr} \sim \bar{\sigma}_{\theta\theta} \sim \gamma h/h_0$ when spatial variation in V_r is neglected. Thus, we expect the crushing kinematics to generate larger compressive stresses at an outer annulus (Fig. 3A, red ring) than at the center because of the larger local film thickness. Regardless of the source of these compressive stresses, surface tension imparts a tensile stress to the liquid sheet that acts to minimize the surface area (Fig. 3D). We believe that the competition of these tensile and compressive stresses is responsible for the location of the wrinkling pattern at a distance L from the center (Fig. 3B). Because the thickness profile is unknown, it is not possible to make a quantitative deduction of the stress field, as would be needed to predict the exact position of the wrinkling pattern. The sheet should remain smooth if surface tension exceeds the compressive stresses throughout the sheet. However, the presence of wrinkles indicates that at a sufficient distance from the center, the

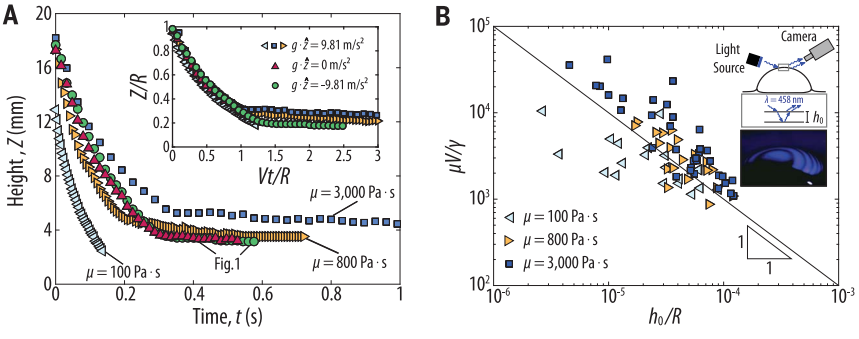

Fig. 2. Effect of bubble film thickness and viscosity on collapse dynamics. (**A**) Measured bubble heights Z versus time t for each orientation and viscosity μ. Inset: The normalized bubble heights Z/R fall onto the same curve when plotted against the dimensionless time Vt/R, highlighting the strong dependence of the collapse speed V on viscosity but not on gravity. (**B**) The collapse speed V is inversely proportional to the measured film thickness h_0, consistent with the notion that surface tension γ drives the collapse. In particular, the experimental results (symbols) suggest that $\mu V/\gamma = 0.1(h_0/R)^{-1}$ (solid line). Here, h_0 is the thickness at the bubble apex, which is estimated using thin-film interferometry (inset).

Downloaded from http://science.sciencemag.org/ on August 6, 2020

compressive stresses dominate those acting to keep the sheet smooth. This behavior is analogous to 1D viscous sheets buckling when the rate of compression is faster than the smoothing effect of surface tension (*11*, *13*). To sidestep the theoretical challenges posed by the thickness variation, we approximate the wrinkled region as an annulus of constant thickness h.

To model the development of the wrinkles, we deduced a dynamic version of the first Föppl–von Kármán equation (*23*, *26*, *27*), which describes the normal force balance along the sheet's center line $\zeta(r, \theta, t)$ as follows (Fig. 3D):

$$\rho h\frac{\partial^2\zeta}{\partial t^2}+\frac{\mu h^3}{3}\nabla^4\left(\frac{\partial\zeta}{\partial t}\right)-\bar{\sigma}_{rr}\frac{\partial^2\zeta}{\partial r^2}-\frac{1}{r^2}\bar{\sigma}_{\theta\theta}\left(\frac{\partial^2\zeta}{\partial\theta^2}+r\frac{\partial\zeta}{\partial r}\right)=2\gamma\nabla^2\zeta \quad (1)$$

where ∇^4 is the biharmonic operator and ∇^2 the Laplacian. Motivated by the observation of multiple radial wrinkles, we sought solutions of the form $\zeta(r, \theta, t) = f(r)\exp(\omega t + in\theta)$. Here, $f(r)$ determines the radial variation of the wrinkle amplitude, ω is the wrinkle growth rate, and n the number of wrinkles. In terms of these parameters, Eq. 1 becomes:

$$\left[\rho h\omega^2 f\right]+\left[\frac{\omega\mu h^3}{3}\left\{\frac{1}{r}\frac{d}{dr}\left(r\frac{d}{dr}\right)-\left(\frac{n^2}{r^2}\right)\right\}^2 f\right]-\left[(\bar{\sigma}_{rr}+2\gamma)\frac{d^2f}{dr^2}+(\bar{\sigma}_{\theta\theta}+2\gamma)\left(\frac{1}{r}\frac{d}{dr}-\frac{n^2}{r^2}\right)f\right]=0 \quad (2)$$

The three square-bracketed terms in Eq. 2 correspond, respectively, to inertia, bending, and compression. Given the high viscosity of the film, one might be tempted to neglect inertial effects. However, the rate of wrinkle development, ω^{-1}, is ~10 ms (Fig. 3E), sufficiently short for the inertial term to become non-negligible. Indeed, for a typical thickness $h \approx 10$ μm, we found the ratio of the inertial and radial compression terms to be of order $\rho h R^2\omega^2/\gamma \sim 1$, justifying the inclusion of inertia in Eq. 1.

When considering axisymmetric film effects, the radial stress $\bar{\sigma}_{rr}$ can have a pronounced role in wrinkling caused by the release of azimuthal stress $\bar{\sigma}_{\theta\theta}$ as the wrinkles develop (*6*). As the dominant stress changes from azimuthal to radial, the dependence on n in the dominant terms of Eq. 2 also changes. Scaling relationships for the growth rate ω and the number of wrinkles n can be obtained from a dominant balance. Specifically, the inertial term scales as $\rho h\omega^2$, the azimuthal bending as $\omega n^4\mu h^3/R^4$, and the radial stress component as γ/R^2. The simultaneous balance of these three dominant terms yields a growth rate $\omega^{-1} \sim \sqrt{\rho h R^2/\gamma}$ and the number of wrinkles $n \sim (2\gamma R^2/\omega\mu h^3)^{1/4}$, or equivalently:

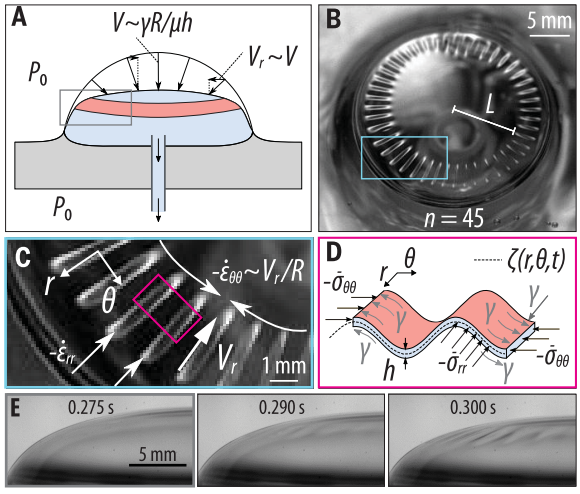

Fig. 3. Mechanism for bubble collapse without rupture. (**A**) Schematic illustrating the experimental setup used to collapse the bubble without rupture. As the bubble collapses, the viscous film obtains a radial velocity V_r proportional to the collapse speed V. (**B**) Wrinkles can still appear without the presence of the hole at a radial distance L from the center. (**C**) Near the periphery of the bubble, the radial and azimuthal compression rates, $\dot{\varepsilon}_{rr}$ and $\dot{\varepsilon}_{\theta\theta}$, respectively, can be related to the radial velocity V_r. (**D**) The azimuthal rate of compression leads to compressive stresses $\bar{\sigma}_{rr}$ and $\bar{\sigma}_{\theta\theta}$, which tend to bend the sheet's centerline $\zeta(r, \theta, t)$ despite being opposed by surface tension γ, which acts to smooth the surface. (**E**) As the bubble collapses, the wrinkles grow and develop within ~25 ms.

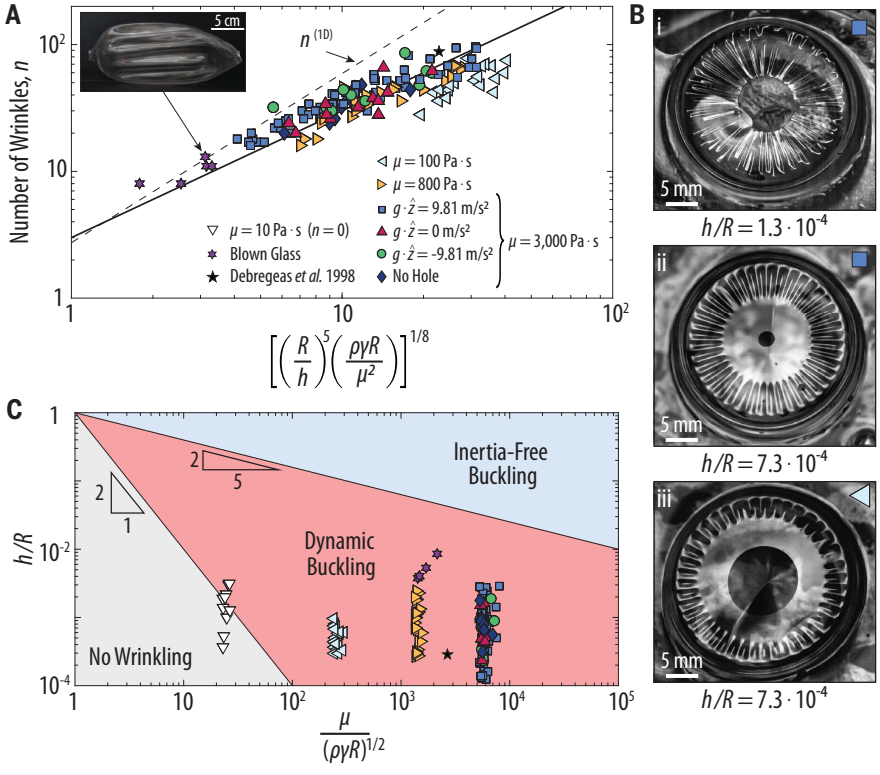

Fig. 4. Comparison of data and model predictions. (**A**) Number of wrinkles n observed on bubbles of various orientations and viscosities is in satisfactory agreement with the scaling of Eq. 3. Wrinkles on blown glass (inset) are also consistent with this trend, although the 1D hoop model (dashed line) is expected to be more appropriate for this nearly cylindrical geometry. (**B**) Top-view images of wrinkled films for: (**i**) viscosity μ = 3000 Pa • s and aspect ratio $h/R = 1.3 \cdot 10^{-4}$, (**ii**) μ = 3000 Pa • s and $h/R = 7.3 \cdot 10^{-4}$, and (**iii**) μ = 100 Pa • s and $h/R = 7.3 \cdot 10^{-4}$. The radial extent of the wrinkles for the thinnest films is limited by the size of the hole, whereas the location L of wrinkles generally increases as the film viscosity decreases. (**C**) Our analysis predicts that inertia is negligible only when $\mu/\sqrt{\rho\gamma R} \gtrsim (R/h)^{5/2}$ (blue region). Because all available data (symbols) are outside of this regime, we incorporated inertial effects into our model. The analysis predicts that there is insufficient growth time for wrinkles to develop when $\mu/\sqrt{\rho\gamma R} \lesssim (R/h)^2$ (gray region), consistent with no wrinkles being observed at the lowest film viscosity (white triangles). Here, the thickness h is computed using the collapse speed V through the relation $h = \gamma R/\mu V$.

Downloaded from http://science.sciencemag.org/ on August 6, 2020

$$n \sim \left[\left(\frac{R}{h}\right)^5 \left(\frac{\rho\gamma R}{\mu^2}\right)\right]^{1/8} \quad (3)$$

To test the scaling of Eq. 3 for the number of wrinkles, we conducted systematic experiments in which we varied the bubble viscosity and orientation while keeping the bubble size confined to the range $0.8 < R < 2$ cm. We also repeated the experiments that involved evacuation rather than puncture of the bubble. We estimated the wrinkled film thickness h using the collapse time $R/V \equiv \mu h/\gamma$, which yields a result that is approximately an order of magnitude larger than the apex thickness h_0 (Fig. 2C). Furthermore, we performed additional experiments with thicker structures by extracting blown molten glass from a furnace and allowing the trapped air to escape through the glass-blowing pipe (*23*). As the air escaped, the blown glass collapsed and adopted a wrinkled shape with thickness $h \approx 200$ μm (Fig. 4A, inset).

The experimental results for the number of wrinkles are illustrated in Fig. 4A. Depending on the initial radius, thickness, and viscosity, the number of wrinkles can range between eight and 96. The experimental results (data points) are in fair agreement with our theoretical prediction (solid line) from Eq. 3. A limitation of our model applies to the data with the thinnest films. For these bubbles, the collapse was so abrupt that the wrinkling pattern lost its symmetry and the wrinkles spanned the entirety of the bubble (Fig. 4Bi). In addition, one should be cautious when interpreting the data for the 100 Pa • s bubble films given the discrepancy evident in Fig. 2B. This discrepancy may stem in part from variations in the thickness profile, which may explain the larger hole size and wrinkle location L observed at this lower viscosity (Fig. 4, Bii and Biii). Note that our analysis is based on the assumption that the wrinkle location L is proportional to the bubble radius and does not account for any dependence of L on film thickness or viscosity.

Our model assumes that the wrinkles develop on an axisymmetric portion of a spherical shell, which may be less appropriate for the blown glass. Specifically, because the molten glass was constantly rotated as it was worked into a thin film, the molten glass bubble (Fig. 4A, inset) assumed the form of a cylindrical shell with roughly hemispherical caps before collapse, and a wrinkled cylinder thereafter. For this case, in solving Eq. 2, we considered a hoop with radius R, where the amplitude f is approximately constant. This approach yields the 1D dynamic buckling dispersion relation $\rho h\omega^2 + \omega\mu h^3 n^4/3R^4 - \bar{\sigma}_{\theta\theta} n^2/R^2 = 0$ (*23*). Linear stability analysis revealed that the most unstable wrinkling pattern is then associated with a growth rate $\omega^{(1D)} \sim (\gamma^2/\rho\mu h^4)^{1/3}$ and a number of wrinkles $n^{(1D)} \sim [(R/h)^5(\rho\gamma R/\mu^2)]^{1/6}$, results analogous to those of Howell (*26*). Although the number of experiments performed with blown glass was insufficient to draw a definitive conclusion, we expect the 1D scaling (Fig. 4A, dotted line) to be more appropriate for this nearly cylindrical geometry. The 2D disk scaling of Eq. 3 is more convincing for all of the data involving the spherical cap bubble geometry.

A prediction of our model is that wrinkling will not occur for all conditions. In both the 1D and 2D scaling, inertia played a critical role in determining the number of wrinkles. Indeed, in both cases, inertia was relevant when $n > 1$, or equivalently $h/R < (\mu/\sqrt{\rho\gamma R})^{-2/5}$, a criterion satisfied by all of our data (Fig. 4C). For the 1D model, had inertia been neglected, the resulting buckled profile would be the equivalent of Euler buckling for a straight beam (*23*). Inertia also appears to dominate the instability growth rate ω: We found no evidence that the viscosity influenced this growth rate time, consistent with our model (*23*). For wrinkles to develop, the time scale for them to grow, $\sqrt{\rho h R^2/\gamma}$, must be less than that of collapse, $\mu h/\gamma$. We thus predict that no wrinkling will occur when $h/R < (\mu/\sqrt{\rho\gamma R})^{-2}$. To test this hypothesis, we ruptured bubbles formed from a silicone oil with viscosity $\mu = 10$ Pa • s (Fig. 4C, white triangles) and indeed found that they did not support any wrinkles.

We have demonstrated that surface tension rather than gravity drives the collapse of viscous surface bubbles after rupture and is likewise responsible for the parachute instability. The capillary-driven collapse initiates a dynamic buckling instability prescribed by the simultaneous interplay of inertia, compression, and viscous bending of the retracting film. Our results suggest that analogous wrinkling is likely to arise on relatively small, curved films, where the effects of gravity are entirely negligible. Equation 1, governing the number of wrinkles, is the viscous counterpart of the elastic Föppl–von Kármán equations used to study the deformation of elastic plates and shells. Our system thus presents an example of viscous sheets exhibiting elastic-like instabilities when rapidly compressed. On the basis of the similar roles played by viscosity and elasticity in these two systems, we can foresee extending our model to systems involving viscoelastic films, in which viscoelastic, capillary, and inertial effects all contribute to the dynamics. For instance, the exhalation of potentially pathogen-bearing aerosols has been linked to the breakup of thin bubble films in the viscoelastic fluid lining of the respiratory tract (*28*, *29*). Our deduction that surface tension alone may prompt buckling during viscous film rupture and retraction suggests the possibility of these films folding and entrapping air, thereby enriching the aerosolization process.

REFERENCES AND NOTES

1. M. B. Hallett, S. Dewitt, *Trends Cell Biol.* **17**, 209–214 (2007).
2. M. Kücken, A. C. Newell, *EPL* **68**, 141–146 (2004).
3. L. Mahadevan, R. Bendick, H. Liang, *Tectonics* **29**, n/a (2010).
4. D. P. Holmes, *Curr. Opin. Colloid Interface Sci.* **40**, 118–137 (2019).
5. J. Huang *et al*., *Science* **317**, 650–653 (2007).
6. B. Davidovitch, R. D. Schroll, D. Vella, M. Adda-Bedia, E. A. Cerda, *Proc. Natl. Acad. Sci. U.S.A.* **108**, 18227–18232 (2011).
7. D. Vella, A. Ajdari, A. Vaziri, A. Boudaoud, *Phys. Rev. Lett.* **107**, 174301 (2011).
8. D. Vella, J. Huang, N. Menon, T. P. Russell, B. Davidovitch, *Phys. Rev. Lett.* **114**, 014301 (2015).
9. H. King, R. D. Schroll, B. Davidovitch, N. Menon, *Proc. Natl. Acad. Sci. U.S.A.* **109**, 9716–9720 (2012).
10. J. Hure, B. Roman, J. Bico, *Phys. Rev. Lett.* **109**, 054302 (2012).
11. G. I. Taylor, in *Proceedings of the Twelfth International Congress of Applied Mechanics, Stanford, 1968* (Springer, 1969), pp. 382–388.
12. J. Teichman, L. Mahadevan, *J. Fluid Mech.* **478**, 71–80 (2003).
13. M. Le Merrer, D. Quéré, C. Clanet, *Phys. Rev. Lett.* **109**, 064502 (2012).
14. M. Kadoura, N. Saranjam, S. Chandra, H. Fan, *Prog. Org. Coat.* **99**, 452–462 (2016).
15. R. Pokorny *et al*., *J. Am. Ceram. Soc.* **98**, 3112–3118 (2015).
16. H. M. Gonnermann, M. Manga, *Annu. Rev. Fluid Mech.* **39**, 321–356 (2007).
17. G. Debrégeas, P.-G. de Gennes, F. Brochart-Wyart, *Science* **279**, 1704–1707 (1998).
18. R. da Silveira, S. Chaıeb, L. Mahadevan, *Science* **287**, 1468–1471 (2000).
19. Y. Toba, *J. Oceanogr. Soc. Jpn* **15**, 121–130 (1959).
20. F. Culick, *J. Appl. Phys.* **31**, 1128–1129 (1960).
21. G. Debrégeas, P. Martin, F. Brochard-Wyart, *Phys. Rev. Lett.* **75**, 3886–3889 (1995).
22. N. Savva, J. W. M. Bush, *J. Fluid Mech.* **626**, 211–240 (2009).
23. See the supplementary materials.
24. N. M. Ribe, *J. Fluid Mech.* **457**, 255–283 (2002).
25. F. T. Trouton, *Proc. R. Soc. London A Contain. Pap. Math. Phys. Character* **77**, 426–440 (1906).
26. P. D. Howell, *Eur. J. Appl. Math.* **7**, 321–343 (1996).
27. S. Bhattacharya, R. V. Craster, M. R. Flynn, *Phys. Fluids* **25**, 043102 (2013).
28. G. R. Johnson, L. Morawska, *J. Aerosol Med. Pulm. Drug Deliv.* **22**, 229–237 (2009).
29. J. B. Grotberg, *Phys. Fluids* **23**, 21301 (2011).

ACKNOWLEDGMENTS

We thank P. Houk for blowing the ultrathin glass bubbles and the referees who urged us to consider a 2D model, which we believe led to a substantially improved manuscript. **Funding:** This work was supported by National Science Foundation grant nos. 1004678 and 1351466 and Office of Naval Research grant no. N00014-16-1-3000. **Author contributions:** A.T.O., J.W.M.B., H.A.S., and J.C.B. designed the study. A.T.O. and J.C.B. conducted the experiments and acquired the data. A.T.O., J.W.M.B., H.A.S., and J.C.B. interpreted the data and proposed mechanical models. A.T.O., J.W.M.B., H.A.S., and J.C.B. contributed equally to the final version of the manuscript. **Competing interests:** The authors declare no competing interests. **Data and materials availability:** All data are available in the main text or the supplementary materials.

SUPPLEMENTARY MATERIALS

science.sciencemag.org/content/369/6504/685/suppl/DC1
Materials and Methods
Figs. S1 to S10
Table S1
References (*30*–*37*)
Movies S1 to S8
Experimental Data Files

12 November 2019; accepted 25 June 2020
10.1126/science.aba0593

Downloaded from http://science.sciencemag.org/ on August 6, 2020

Science

A new wrinkle on liquid sheets: Turning the mechanism of viscous bubble collapse upside down

Alexandros T. Oratis, John W. M. Bush, Howard A. Stone and James C. Bird

Science **369** (6504), 685-688.
DOI: 10.1126/science.aba0593

Slower-motion bubble collapse

The collapse of viscous bubbles is of practical interest to geophysics, glass manufacturing, and food processing. Previous studies have suggested that gravity or small punctures may play a role in the wrinkling and collapse of viscous bubbles. By studying bubbles with a range of viscosity and by tilting them both sideways and upside down, Oratis *et al.* conclude that gravity is not a factor. Instead, surface tension and dynamic stress of the compressed liquid seem to be the main driving mechanisms for the behavior of the bubbles and the wrinkling instability.

Science, this issue p. 685

ARTICLE TOOLS http://science.sciencemag.org/content/369/6504/685

SUPPLEMENTARY MATERIALS http://science.sciencemag.org/content/suppl/2020/08/05/369.6504.685.DC1

REFERENCES This article cites 36 articles, 5 of which you can access for free
http://science.sciencemag.org/content/369/6504/685#BIBL

PERMISSIONS http://www.sciencemag.org/help/reprints-and-permissions

Use of this article is subject to the Terms of Service

Science (print ISSN 0036-8075; online ISSN 1095-9203) is published by the American Association for the Advancement of Science, 1200 New York Avenue NW, Washington, DC 20005. The title *Science* is a registered trademark of AAAS.

Copyright © 2020 The Authors, some rights reserved; exclusive licensee American Association for the Advancement of Science. No claim to original U.S. Government Works

Downloaded from http://science.sciencemag.org/ on August 6, 2020

science.sciencemag.org/content/369/6504/685/suppl/DC1

Supplementary Materials for

A new wrinkle on liquid sheets: Turning the mechanism of viscous bubble collapse upside down

Alexandros T. Oratis, John W. M. Bush, Howard A. Stone, James C. Bird*

*Corresponding author. E-mail: jbird@bu.ed

Published 7 August 2020, *Science* **369**, 685 (2020)
DOI: 10.1126/science.aba0593

This PDF file includes:

Other Supplementary Material for this manuscript includes the following:
(available at science.sciencemag.org/content/369/6504/685/suppl/DC1)

Movies S1 to S8 (.mp4 files)
Experimental Data S1 to S3 (Excel files)

Materials and Methods

Silicone oil selection and independent viscosity measurements

Five different viscosity silicone oils were purchased (Clearco Products Co Inc.) to complete the experiments. These were selected based on their labeled kinematic viscosity: $\nu = 10,000$ cSt, 100,000 cSt, 600,000 cSt, 1,000,000 cSt, and 2,500,000 cSt. As the difference in these silicone oils is the average chain length of the polymer melt, the density and surface tension remain constant between the different oils at $\rho = 970$ kg/m^3 and $\gamma = 0.02$ N/m, respectively.

Given that precise values of the viscosity are necessary, we performed experiments where we dropped stainless steel spheres of radius $a = 1.5$ mm in each silicone oil and measured the sphere's terminal velocity U. The spheres were gently dropped at the center of a cylindrical tank with radius 75 mm and height 12 mm to ensure the side and bottom walls did not affect the speed measurements. Based on Stokes' law, the viscous drag should equal $F_D = 6\pi\mu U a$, where $\mu = \rho\nu$ is the dynamic viscosity. Balancing the viscous drag with weight of the sphere $F_W = \frac{4}{3}\pi a^3 \rho_s g$ and the buoyancy force $F_B = \frac{4}{3}\pi a^3 \rho g$, such that $F_D = F_W - F_B$, yields a relation for the dynamic viscosity $\mu = \frac{2}{9}(\rho_s - \rho) g a^2 / U$. Here, $\rho_s = 8.0 \cdot 10^3$ kg/m^3 is the sphere's density and $g = 9.8$ m/s^2 the acceleration due to gravity. The experimentally measured dynamic viscosities are tabulated in Table S1.

Method of bubble creation

We prepare the viscous bubble films by first pouring the silicone oil into a petri dish. Air was injected into the silicone oil bath, and rose to the surface to form a bubble. The corresponding bubble radii ranged between 0.8 and 2 cm, thus exceeding the capillary length $\sqrt{\gamma/\rho g} \approx 0.1$ cm, causing the bubble to protrude substantially beyond the surface and form a hemispherical dome. After waiting for a sufficiently long time to allow gravitational drainage to thin the

bubble walls, we puncture the bubble at the top with a sharp needle, and record the subsequent collapse at frame rates ranging between 250-1,000 frames per second, depending on the film's viscosity. Two high-speed cameras (Photron SA-5 and Photron SA-X2) were used, one positioned on the side to record the collapse and the other on top of the bubble to record the wrinkling characteristics.

Method to reorient bubbles

For the experiments where the viscous bubble film is punctured in an upside-down or sideways orientation, the petri dish was clamped to a rotatable frame (Fig. S1). Air was first injected in the upright configuration so that gravity can shape the bubble (Fig. S1A). The petri dish was then rapidly rotated to the desired orientation (Fig. S1B,C), and the bubble punctured within seconds. Because the viscosity is sufficiently large, the silicone oil did not flow out of the dish during reorientation and the bubble could still be punctured.

Method to measure bubble collapse velocity and morphology

To measure the collapse velocity and other morphological features of a bubble, we developed custom image processing algorithms. We describe these below using a bubble shown in the main text (Fig. 1C) as a representative example.

The height of bubble film above the flat interface is measured directly from the high-speed images. For all experiments, we track the height Z of the bubble center ($r = 0$) over time t for the duration of the bubble collapse. From this data, we calculate a collapse time and a characteristic collapse velocity V (Fig. S2). We can also calculate the height of the film at other radial positions ($0 < r < R$) for each image during the collapse to map the evolution of the bubble shape. A collection of these shapes, corresponding to the bubble in Fig. 1C of the main text, is illustrated in Fig. S2A. Note that the position of the film and growing hole have been

averaged for a given radius so that the curves are axisymmetric. During the final stages of the sideways collapse, weak gravitational effects lead to a slight shape asymmetry, highlighting the requirement for rapid rotation and rupture.

It is difficult to measure the shape of the interface below the bubble, however we can approximate it with theory based on the Bond number $Bo = \rho g R^2/\gamma = 100$ prior to the re-orientation (*19*). This theoretical shape is plotted on top of the measurements (dashed lines in Fig. S2A). The theoretical shape allows us to identify the location and extent of the bubble meniscus, and it is noteworthy that the rapid change in curvature and wrinkling occurs within the film cap above this meniscus.

The shapes of the bubble can be used to extract various properties, such as the surface area and curvature, that will enhance our understanding of the underlying dynamics. However, measurement noise in the curve positions is accentuated during numerical differentiation, and therefore we find it advantageous to first smooth these extracted points. Specifically, we fit the experimental bubble shapes with smooth empirical curves of the form:

$$\frac{z}{L} = \left[1 - \left(\frac{r}{R}\right)^2\right]^{1/N} \tag{S1}$$

Note that $N = 2$ corresponds to the shape of a circle. Here, we empirically fit N to the shapes and find that its value varies between 2.2 and 4. The comparison between the experimental shapes and the fit curves is illustrated in Fig. S2A. On these curves, we can track the edge of the growing hole and the height of the apex (dots and triangles in Fig. S2B).

The height at the center of the film can be estimated directly from the shapes and does not require smoothing. This height $Z(t)$ typically decreases faster at early times and then decelerates as it reaches the midpoint of the collapse and then reaches a much slower phase of its evolution at around 20% of the original height (Fig. S2C). The meniscus may play a role in setting this height, yet the bubble shape did not change significantly enough to warrant deeper

exploration at this time. We plot the bubble height against time to extract an average collapse speed V. Because wrinkling typically occurs when $Z/R \approx 0.6$, we use this value to set the time interval used to compute the collapse speed. Specifically, we use a linear fit for the height Z with time in the interval $0.6 < Z/R < 1$, from which we can compute the collapse speed through the slope of the fit. With the approximate shape of the collapsing bubble (Eq. (S1)), we can compute the curvature and the surface area of the bubble film, as well as the rate of internal volume change. In particular, the surface area S at a point in time can be computed by numerically evaluating the surface of revolution

$$S = 2\pi \int r(z)\sqrt{\left(1 + [dr/dz]^2\right)}dz, \tag{S2}$$

and the volume of the air within the bubble can be computed with the solid of revolution

$$\Omega = \pi \int r(z)^2 dz. \tag{S3}$$

Meanwhile twice the mean curvature $\mathcal{H} = \kappa_1 + \kappa_2$ can be computed from the two principal curvatures:

$$\kappa_1 = \frac{d^2z/dr^2}{\left[1 + [dz/dr]^2\right]^{3/2}}, \tag{S4}$$

$$\kappa_2 = \frac{dz/dr}{r\sqrt{1 + [dz/dr]^2}}. \tag{S5}$$

From this analysis, we observe that the overall surface area of the bubble decreases monotonically, consistent with surface-tension driving the collapse (Fig. S2D). The volume of the air within the bubble is also decreasing with time. Here the collapse is consistent with an exiting flow rate of $Q \approx 60$ mL/s (Fig. S2E). If the collapse were quasi-static so that the surface area were minimized at each point in time, the shapes in Fig. S2A would form a series of spherical caps (*30*). However, we observe that the film curvature varies spatially, resulting in a mean curvature that increases near the base of the bubble (Fig. S2F). We attribute this variation to the

film become progressively thicker from the apex to the bubble base. These observations are consistent with the notion that surface tension is driving the collapse globally, but that varying viscous stresses, due to variation in thickness, are frustrating the collapse locally.

Methods to estimate thickness

A crucial variable for the collapse dynamics is the thickness of the film surrounding bubble, which we are unable to measure during the collapse. However, we can estimate the thickness at the apex h_0 prior to the collapse by using a combination of interferometry and drainage theory. Note that this thickness is significantly less than the thickness where the wrinkling instability occurs; however, there is precedent to believe that the drainage-profile is self-similar such that the thickness at a particular distance from the top is proportional to the instantaneous apex thickness (*17*).

Rate of drainage from interferometry

We use thin-film interferometry to measure the drainage rate at the top of the bubble. Specifically, we shine monochromatic light (SugarCUBE LED Illuminator) of known wavelength $\lambda = 458$ nm on the bubble at a shallow angle and record the reflection with a camera (Fig. S3A). The light reflects from both the top and bottom of the film and, depending on the film thickness, these two reflections can constructively or destructively interfere. Although we focus on the thickness at the top, interference fringes propagate from the bubble's apex, causing the intensity to vary (Fig. S3B). Here we assume that the index of refraction of the silicone oil (n_f=1.4) exactly balances out the effect of the internal angle, which corresponds to the light shining on the film at an oblique angle between 10 to 20 degrees from the horizontal. With this simplifying assumption, the light constructively interferes whenever the film thickness is a multiple of $\lambda/2$. A snapshot of the bubble under the glancing blue light reveals concentric blue rings centered

from the bubble apex (Fig. S3B), highlighting that the film thickness is axisymmetric as it varies between the top and base of the bubble. Focusing just at the top of the bubble, we find that the light intensity oscillates with time until the bubble is ruptured at time t_0 (Fig. S3C). From the time series, we assume that each of the peaks corresponds to constructive interference and each of the valleys corresponds to destructive interference, from which we can estimate the time rate of change in thickness $dh/dt \approx \Delta h/(\Delta t) = \lambda/(2\Delta t)$ (Fig. S3D). If we repeat this process for an upside-down bubble, we get similar interference patterns, although the amplitude of the intensity decreases with time, which is consistent with the film thickness increasing rather than decreasing (Fig. S3E). From the time between successive peaks (circles) and successive valleys (exes), we conclude that the film thickens at a similar rate to which it drains under the influence of gravity (Fig. S3F). This rate is on the order of tens of nanometers per second for the representative bubbles illustrated here.

Combining interferometry and drainage theory

Debregeas et. al. (*17*) also measured thickness at the top of draining silicone oil bubbles using thin-film interferometry. However in their study, they were not rupturing the films and therefore could collect interferometry data to the point of a black film, which provided an absolute reference point. They found that the thickness at the top of the bubble followed an exponential decay with timescale $\tau_d \sim \mu/\rho g R$, as predicted by their drainage model (*17*). Thus we can write an expression for the film thickness as

$$h_{top} = h_0 \exp\left(-\frac{t - t_0}{\tau_d}\right), \tag{S6}$$

where h_0 is the thickness at the point of rupture t_0.

Because we do not have an absolute thickness to reference our film measurements, our approach is to consider the rate of drainage. Differentiating Eq. (S6) with respect to time, the

drainage rate follows

$$\frac{dh_{top}}{dt} = -\frac{h_0}{\tau_d} \exp\left(\frac{t_0 - t}{\tau_d}\right). \tag{S7}$$

This exponential decrease in drainage rate is consistent with our interferometry results (Fig. S3D). By fitting an exponential to these data points, we can calculate both τ_d and h_0. The exponential fit for the particular data in Fig. S3D corresponds to a time constant $\tau = 74.8$ s and a top thickness $h_0 = 0.88\,\mu\mathrm{m}$ at rupture. In this particular case, the bubble radius was $R = 15.7$ mm and the viscosity $\mu = 3000$ Pa s. Therefore the value of τ obtained from the fit is consistent to the value that would be predicted from the measurements and theory of Debregeas et. al. (*17*), noting a scaling prefactor of approximately 17 that can be observed in their data.

Method to collapse bubbles without rupture

For the experiments involving the bubble collapse without puncture, a small opening was created at the bottom of the petri dish. A long steel needle connected to a syringe through a valve was inserted into the opening to insert air. The size of the opening was set to match the needle diameter. As the air rose to the surface to form the dome, the needle followed the bubble in order to create a channel with the sealed valve. When the dome walls were sufficiently thin, the valve was quickly opened, allowing the pressurized air beneath the bubble cap to escape. The normalized bubble height Z against time scaled by the collapse speed V for the bubble without a hole is illustrated in Fig. S4, and follows a similar collapse with a punctured bubble of the same viscosity.

Extension to molten blown glass

The molten glass experiments were conducted at the Glass Lab at MIT. Soda-lime glass was melted inside a main furnace, heated at approximately 900° C. A blob of the molten glass was attached to a blowpipe, through which air was blown to develop a cylindrical structure. The

molten glass structure was worked into thin walls by repeatedly blowing, working and reheating in a secondary furnace heated at the same temperature as the first. Once the walls were deemed sufficiently thin, the blowpipe exit hole was closed and the glass cylinder brought into a furnace to reheat. At this point, the exit hole of the blowpipe was released, allowing the pressurized air to escape. Wrinkles developed on the blown glass, which was then placed inside a third chamber, allowing it to gradually cool and stiffen.

The resulting wrinkled blown glass is illustrated in Fig. S5. The remaining structures used in Fig. 4 of the main text, are shown in Fig. S6. Based on the furnace temperature of approximately 900° C, the molten soda-lime glass viscosity, surface tension and density used in our analysis were $\mu \approx 10,000$ cP, $\gamma \approx 0.37$ N/m and $\rho \approx 2.7$ g/cm^3 respectively (*31, 32*).

Theory and Scaling

Theoretical rationale for velocity scaling

In this section, we obtain a characteristic velocity $\frac{\gamma R}{\mu h_0}$ by modeling the speed that a spherical viscous film would collapse driven by surface tension and regulated by viscosity. As modeled by van der Fliert et al. (*30*), a free-surface spherical shell with with radius r and thickness h will contract when an external pressure ΔP is exerted upon it. In particular, the conservation of mass and momentum can be described by the following equations:

$$\frac{d}{dt}(r^2 h) = 0, \tag{S8}$$

$$\frac{dr}{dt} = \frac{r^2 \Delta P}{12 \mu h}. \tag{S9}$$

Because surface tension is the force driving the collapse of the spherical shell, the external pressure can be related to the Laplace pressure $\Delta P = -4\gamma/r$. Substituting the Laplace pressure into Eqs. (S8)-(S9) and combining the initial conditions $r(0) = R$ and $h(0) = h_0$, we obtain the

following equations for the behavior of the contracting spherical shell:

$$\frac{r}{R} = \left(1 + \frac{2\gamma t}{3\mu h_0}\right)^{-1/2}, \tag{S10}$$

$$\frac{h}{h_0} = 1 + \frac{2\gamma t}{3\mu h_0}. \tag{S11}$$

Therefore the velocity that the sphere collapses inward is

$$-\frac{dr}{dt} = \frac{V_c}{3}\left(1 + \frac{2\gamma t}{3\mu h_0}\right)^{-3/2}, \tag{S12}$$

where the characteristic velocity is $V_c = \frac{\gamma R}{\mu h_0}$. In our system, both the downward velocity V and the resulting radial velocity V_r are expected to scale as this characteristic velocity V_c.

Föppl-von-Kármán equations for a viscous disk

We develop here a basic theoretical framework that allows us to analyze the stress distribution on thin viscous sheets, drawing from established analogies with thin elastic sheets (*6, 9, 26*). A key difference between elastic and viscous sheets, is that elastic sheets are described in terms of strains, while viscous sheets in terms of the rate of strain. Because the viscous bubble in our experiments is most easily described in terms of a circular geometry, we use a set of polar coordinates r, θ (Fig. S7). The components of the rate of strain tensor $\dot{\varepsilon}_{rr}$, $\dot{\varepsilon}_{\theta\theta}$ and $\dot{\varepsilon}_{r\theta}$ are related to the radial and azimuthal velocities v_r and v_θ, as well as the centerline of the sheet $\zeta(r, \theta, t)$:

$$\dot{\varepsilon}_{rr} = \frac{\partial v_r}{\partial r} + \frac{\partial \zeta}{\partial r}\frac{\partial^2 \zeta}{\partial r \partial t}, \tag{S13a}$$

$$\dot{\varepsilon}_{\theta\theta} = \frac{v_r}{r} + \frac{1}{r}\frac{\partial v_\theta}{\partial \theta} + \frac{1}{r^2}\frac{\partial \zeta}{\partial \theta}\frac{\partial^2 \zeta}{\partial \theta \partial t}, \tag{S13b}$$

$$\dot{\varepsilon}_{r\theta} = \frac{1}{r}\frac{\partial v_r}{\partial \theta} + \frac{\partial v_\theta}{\partial r} + \frac{1}{r}\frac{\partial \zeta}{\partial r}\frac{\partial^2 \zeta}{\partial \theta \partial t} + \frac{1}{r}\frac{\partial \zeta}{\partial \theta}\frac{\partial^2 \zeta}{\partial r \partial t}. \tag{S13c}$$

The rates of strain are related to the components of the 2D stress tensor $\bar{\sigma}$ through constitutive relations based on a Trouton model (*25, 26*) and analogous to Hooke's law:

$$\bar{\sigma}_{rr} = 2\mu h \left(2\dot{\varepsilon}_{rr} + \dot{\varepsilon}_{\theta\theta}\right), \tag{S14a}$$

$$\bar{\sigma}_{\theta\theta} = 2\mu h \left(\dot{\varepsilon}_{rr} + 2\dot{\varepsilon}_{\theta\theta}\right), \tag{S14b}$$

$$\bar{\sigma}_{r\theta} = \mu h \dot{\varepsilon}_{r\theta}, \tag{S14c}$$

where μ is the viscosity of the fluid, h its thickness, and the overbar over the stress is to highlight that the 3D stress has been integrated over the thickness. The system is fully characterized by the force balance in the radial and azimuthal direction through $\nabla \cdot \bar{\sigma} = P_R\hat{r} + P_\theta\hat{\theta}$ and in the normal direction by $(\mu h^3/3)\nabla^2 \mathrm{Tr}(\dot{\kappa}) + \bar{\sigma} \cdot \kappa = P_N$. Here $\mathrm{Tr}(\dot{\kappa})$ is the trace of the time rate of change of the curvature tensor κ and P_N the external normal force per area exerted on the viscous sheet. The importance of the rate compression rather than mere compression for viscous bending, is exemplified by the analogy in the bending term between elastic and viscous sheets $E\kappa \Leftrightarrow \mu\dot{\kappa}$, where E is the Young's modulus (*13*). Thus, these equations are analogous to the Föppl-von-Kármán equations in elasticity theory and can be expressed in polar coordinates as:

$$\hat{r} : \frac{\partial \bar{\sigma}_{rr}}{\partial r} + \frac{1}{r}\left(\frac{\partial}{\partial \theta}\bar{\sigma}_{r\theta} + \bar{\sigma}_{rr} - \bar{\sigma}_{\theta\theta}\right) = P_R, \tag{S15a}$$

$$\hat{\theta} : \frac{\partial \bar{\sigma}_{r\theta}}{\partial r} + \frac{1}{r}\left(\frac{\partial}{\partial \theta}\bar{\sigma}_{\theta\theta} + 2\bar{\sigma}_{r\theta}\right) = P_\theta, \tag{S15b}$$

$$\frac{\mu h^3}{3}\nabla^4\left(\frac{\partial \zeta}{\partial t}\right) - \bar{\sigma}_{rr}\frac{\partial^2 \zeta}{\partial r^2} - \frac{2}{r}\bar{\sigma}_{r\theta}\left(\frac{\partial}{\partial r} - \frac{1}{r}\right)\frac{\partial \zeta}{\partial \theta} - \frac{1}{r^2}\bar{\sigma}_{\theta\theta}\left(\frac{\partial^2 \zeta}{\partial \theta^2} + r\frac{\partial \zeta}{\partial r}\right) = P_N, \tag{S15c}$$

where the 2D Laplacian is given by $\nabla^2 = \left(\frac{\partial^2}{\partial r^2} + \frac{1}{r}\frac{\partial}{\partial r} + \frac{1}{r^2}\frac{\partial^2}{\partial \theta^2}\right)$, the biharmonic by $\nabla^4 = \left(\frac{\partial^4}{\partial r^4} + \frac{2}{r}\frac{\partial^3}{\partial r^3} - \frac{1}{r^2}\frac{\partial^2}{\partial r^2} + \frac{1}{r^3}\frac{\partial}{\partial r} + \frac{2}{r^2}\frac{\partial^4}{\partial \theta^2 \partial r^2} - \frac{2}{r^3}\frac{\partial^3}{\partial \theta^2 \partial r} + \frac{4}{r^4}\frac{\partial^2}{\partial \theta^2} + \frac{1}{r^4}\frac{\partial^4}{\partial \theta^4}\right)$ and P_R and P_θ are typically zero. We can further simplify Eq. (S15c) by assuming axisymmetry, so that $v_\theta = \dot{\varepsilon}_{r\theta} = 0$, $\dot{\varepsilon}_{rr} = \partial v_r/\partial r$ and $\dot{\varepsilon}_{\theta\theta} = v_r/r$. In addition, the externally applied normal force P_N in our system is due to surface tension and can be expressed as $2\gamma\nabla^2\zeta$, where the 2 arises because surface

tension acts on both sides of the sheet. Finally, we consider the inertia of the sheet to play an important role, which when included in Eq. (S15c) reduces to:

$$\rho h \frac{\partial^2 \zeta}{\partial t^2} + \frac{\mu h^3}{3} \nabla^4 \left(\frac{\partial \zeta}{\partial t} \right) - \bar{\sigma}_{rr} \frac{\partial^2 \zeta}{\partial r^2} - \frac{1}{r^2} \bar{\sigma}_{\theta\theta} \left(\frac{\partial^2 \zeta}{\partial \theta^2} + r \frac{\partial \zeta}{\partial r} \right) = 2\gamma \nabla^2 \zeta, \tag{S16}$$

where ρ is the density of the fluid. Note that in the theory of wrinkling of elastic solids, inertia does not traditionally play a role since the systems considered are typically quasi-static (*6, 7, 9*). However for rapid compression, inertia can excite higher-order modes, a phenomenon often referred to as dynamic buckling.

In the subsections below, we aim to describe the wrinkling of our viscous film in terms of analysis developed for static elastic disks and rapidly deformed slender objects, for which inertia can play a role. We conclude by suggesting that both confinement and inertia are important in setting the number of wrinkles for the collapsing viscous bubbles. A key point in our interpretation is that the extent of wrinkles L is connected to the variation in the film thickness: the wrinkles closer to the center smooth out faster than wrinkles further from the center. The contribution of surface tension in Eq. (S16) can be rearranged with each stress component to highlight that importance of net stresses $(-\bar{\sigma}_{rr} - 2\gamma)$ and $(-\bar{\sigma}_{\theta\theta} - 2\gamma)$. Based on our scaling for the radial speed $V_r \sim V \sim \gamma R/\mu h_0$, the stresses simplify to $\bar{\sigma}_{rr} \sim \bar{\sigma}_{\theta\theta} \sim \gamma h/h_0$. Therefore, for the same inward velocity, the thickness-integrated stress increases as film get thicker toward the periphery of the bubble, and reaches a point L where they overcome the smoothing effects of surface tension. Provided that the thickness in this region h scales with h_0, the net stress components, $(\bar{\sigma}_{rr} + 2\gamma)$ and $(\bar{\sigma}_{\theta\theta} + 2\gamma)$ scale as γ, with a prefactor that depends on the local thickness and inward velocity.

At first glance, it may seem that the shape of the film should be determined from the integrated stress from the kinematics without also considering the counteracting smoothing effects of surface tension. This perspective is supported by recent observations that the integrated stress

across a floating elastic sheet is equal to the liquid-vapor surface tension pulling on its boundary and independent of the interfacial tensions of the elastic sheet (*33*). However, we do not believe that these results for elastic films directly carry over to the liquid films, as the stress-free state of the film is fundamentally different. Indeed, the paper by Le Merrer et al. (*13*) provides experimental evidence that the curvature of a viscous liquid film depends on both an integrated stress applied at the boundary and the interfacial tension on the film. Furthermore, this paper highlights two criteria for buckling for viscous liquids: first, the aspect ratio has to be sufficiently thin and, second, the timescale of compression has to be short relative to the timescale required for surface tension to smooth the surface. In all of our films, $h << R$ and the first criterion is met. It is the second criteria that we believe is responsible for the thinner center of our films ($r < L$) remaining smooth while the thicker annular region ($L < r < R$) wrinkles. To illustrate this point, we consider what happens to the wrinkles after the film collapse (Fig. S8). Once collapsed, there is no longer a downward or inward velocity, and therefore there are no longer viscous stresses associated with the film motion. Thus, surface tension acts unopposed, removing excess surface area and relaxing the wrinkles. The length of the smooth inner-circle L increases with time, as is consistent with wrinkles of thinner film smoothening faster than wrinkles of thicker film.

Inertia-free wrinkle analysis

Recognizing some similarities between the viscous film and wrinkles in stretched, elastic axisymmetric films, we follow a similar approach to model the wrinkling. We first neglect inertial effects. The film centerline takes the form $\zeta(r,\theta,t) = f(r)\exp(\omega t + in\theta)$, so the general equation (S16) reduces to the viscous Föppl-von-Kármán equation:

$$\frac{\omega\mu h^3}{3}\left\{\frac{1}{r}\frac{\mathrm{d}}{\mathrm{d}r}\left(r\frac{\mathrm{d}}{\mathrm{d}r}\right)-\frac{n^2}{r^2}\right\}^2 f-(\bar{\sigma}_{rr}+2\gamma)\frac{\mathrm{d}^2 f}{\mathrm{d}r^2}-(\bar{\sigma}_{\theta\theta}+2\gamma)\left(\frac{1}{r}\frac{\mathrm{d}}{\mathrm{d}r}-\frac{n^2}{r^2}\right)f=0. \quad \text{(S17)}$$

Here, n represents the number of wrinkles and ω the growth rate. To initiate radial wrinkles, we anticipate the azimuthal stress to exceed the radial stress at the onset of wrinkling (*6*). Yet, far from this instability threshold, the buckling allows the azimuthal stress to relax and decrease significantly. Therefore, the dominant terms in Eq. (S17) are the viscous bending and the radial stress, which scale $\mu h^3 \omega / R^4$ and γ / R^2 respectively. Balancing these dominant terms does not immediately provide an expression for the number of wrinkles, since there are two unknowns: n and ω. This challenge does not appear in the corresponding analysis for elastic sheets, due to the absence of the growth rate in the associated bending stiffness. If the only natural timescale within the system is the collapse time, then the growth rate ω would be expected to scale as $\gamma / \mu h$. Combining this assumption with the balance of bending and radial stress, yields the following result for the number of wrinkles:

$$n \sim \left(\frac{R}{h} \right)^{1/2} \tag{S18}$$

It is noteworthy that the result for the number of wrinkles n depends purely on geometry and not on any material properties. Yet, this result is obtained based on the assumption that the growth rate occurs at a similar time scale to the bubble collapse. Careful inspection of wrinkling instability (Fig. 3E), suggests that the wrinkles develop at a time scale on the order of 10 ms, which is an order of magnitude smaller than the assumed growth rate. We believe that this discrepancy is due to another timescale entering into the problem, specifically inertia.

Dynamic viscous buckling

To illustrate why we believe it necessary to account for inertia in Eq. (S16), we consider a slightly simplified scenario. Specifically, in the middle of the wrinkling region, we assume that the deformation ζ does not vary with r so that $\zeta = \zeta(\theta, t)$ and Eq. (S16) reduces to

$$\rho h \frac{\partial^2 \zeta}{\partial t^2} + \frac{(-\bar{\sigma}_{\theta\theta} - 2\gamma)}{r^2} \frac{\partial^2 \zeta}{\partial \theta^2} + \frac{\mu h^3}{3 r^4} \left[\frac{\partial^5 \zeta}{\partial t \partial^4 \theta} \right] = 0. \tag{S19}$$

Equation (S19) bears similarities with the dynamic buckling equation for elastic beams and rods (*34-37*). In particular, if $r\partial\theta$ is replaced by ∂x and $\mu\frac{\partial}{\partial t}$ is replaced by $E/4$, where E is the Young's modulus, one obtains the dynamic buckling equation $\rho h\zeta_{tt} + F\zeta_{xx} + (Eh^3/12)\zeta_{xxxx} = 0$.

The solution of Eq. (S19) depends strongly on the sign of the second term, which is prescribed by the relative magnitude of the compressive stress and surface tension. In our system, the compressive stress is also driven by surface tension through the bubble collapse, so it is expected that the collective contribution scales as the surface tension. Seeking solutions to Eq. (S19) of the form $\zeta = \zeta_0 \exp(\omega t + in\theta)$, linear stability analysis for $(-\bar{\sigma}_{\theta\theta} - 2\gamma) \sim \gamma > 0$ then yields scaling relations for the number of wrinkles n and associated growth rate ω of the most unstable mode:

$$n \sim \left(\frac{R}{h}\right)^{5/6} \left(\frac{\rho\gamma R}{\mu^2}\right)^{1/6} \quad \text{and} \quad \omega \sim \left(\frac{\gamma^2}{h^4\mu\rho}\right)^{1/3}. \tag{S20}$$

Here, for simplicity, we are assuming that the radius r for which the wrinkles develop is R. Had inertia been neglected, there would be only one buckle; a result equivalent to Euler-Buckling for a straight beam. Inertia becomes relevant as soon as $n > 1$, or when

$$h/R < \left(\mu/\sqrt{\rho\gamma R}\right)^{-2/5}. \tag{S21}$$

This relationship defines the boundary between Dynamic Buckling and Inertia-free Buckling in Fig. 4A of the main text. There are immediate parallels with this analysis and that carried out for 1-D planar viscous sheets by Howell (*26*). In particular, the analysis could be viewed as indicating that a characteristic velocity $V \sim \gamma R/\mu h$ reduces the perimeter of the wrinkled hoop. Thus the number of wrinkles in Eq. (S20) is equivalent to $n \sim (R/h)^{2/3}\mathrm{Re}^{1/6}$, where $\mathrm{Re} \equiv \rho V R/\mu$ is the Reynolds number. Similarly the condition for inertia to be relevant to the number of wrinkles (Eq. (S21)), can be expressed as:

$$\frac{h}{R} < \left(\frac{\rho V R}{\mu}\right)^{1/4}, \tag{S22}$$

a relationship pointed out by Howell (*26*). Typical values for the Reynolds number in our experiments span the range $10^{-6} \lesssim \mathrm{Re} \lesssim 10^{-1}$, which is large enough to justify the inclusion of inertial effects given the typical aspect ratio $h/R \sim 10^{-3}$ in our experiments. This criterion provides a context to relate our experiments to those in which a viscous thread is subjected to an imposed external velocity. Figure S9 highlights the fact that the experiments by Le Merrer et. al. (*13*) were performed in a predominantly inertia-free regime; whereas, our experiments are in the regime where inertia is relevant.

Scaling for film disk with inertia

Returning to the viscous disk geometry, we now consider the role of inertia in the wrinkle dynamics. We again assume a wrinkled profile $\zeta(r,\theta,t) = f(r)\exp(\omega t + in\theta)$, where ω is the instability growth rate and n the number of wrinkles, and express Eq. (S15c) in terms of these variables.

$$\rho h\omega^2 f + \frac{\omega\mu h^3}{3}\left\{\frac{1}{r}\frac{\mathrm{d}}{\mathrm{d}r}\left(r\frac{\mathrm{d}}{\mathrm{d}r}\right) - \frac{n^2}{r^2}\right\}^2 f - (\bar{\sigma}_{rr} + 2\gamma)\frac{\mathrm{d}^2 f}{\mathrm{d}r^2} - (\bar{\sigma}_{\theta\theta} + 2\gamma)\left(\frac{1}{r}\frac{\mathrm{d}}{\mathrm{d}r} - \frac{n^2}{r^2}\right) f = 0 \tag{S23}$$

Therefore, the inertial term will scale as $\sim \rho h\omega^2$, the bending term $\sim \mu h^3 n^4 \omega/R^4$ and the radial stress $(\bar{\sigma}_{rr} + 2\gamma)/R^2$. Because the azimuthal stress relaxes at the onset of wrinkling, we again neglect it for this 2D analysis. Balancing these three terms yields a growth rate $\omega^{-1} \sim \sqrt{\rho h R^2/\gamma}$, and number of wrinkles $n \sim (2\gamma R^2/\omega\mu h^3)^{1/4}$. Combining these two results yields a scaling for the number of wrinkles:

$$n \sim \left(\frac{h}{R}\right)^{-5/8}\left(\frac{\mu}{\sqrt{\rho\gamma R}}\right)^{-1/4} \tag{S24}$$

This analysis predicts that wrinkles should develop quite quickly relative the collapse time. More specifically, for a bubble in silicone oil with $R \approx 1$ cm and $h \approx 10\,\mu$m, the time for

wrinkles to develop should be on the order of $\omega^{-1} \sim \sqrt{\rho h R^2/\gamma}$ ~10 ms. Figure S10 shows snapshots of the bubble collapse, which indicate the relevance of this timescale in the wrinkling process. Furthermore when higher-speed images were collected for silicone oils of different viscosity, there was no evidence that viscosity influenced the wrinkle-development time, consistent with the model scaling for ω. Finally, for wrinkles to develop, they must have enough time to develop before the film fully collapses. Based on our model, wrinkles should only be observed if $\omega^{-1} < R/V$, which is equivalent to $\sqrt{\rho h R^2/\gamma} < \mu h/\gamma$ or

$$h/R > \left(\mu/\sqrt{\rho\gamma R}\right)^{-2}. \tag{S25}$$

This relationship defines the boundary between No Wrinkling and Dynamic Buckling in Fig. 4A of the main text. Notably, no wrinkling is observed for any of the experiments conducted in this regime.

Table S1: For each labeled kinematic viscosity in cSt (1 cSt = $10^{-5}\ \mathrm{m}^2/\mathrm{s}$), we measure the solid sphere's terminal velocity U and the corresponding computed dynamic viscosity μ.

Labeled ν (cSt)	U (μm/s)	Computed μ (Pa·s)
10^4	2,640 $\pm$ 200	12.6 $\pm$ 0.9
10^5	245 $\pm$ 2	136 $\pm$ 2
$6 \cdot 10^5$	43.2 $\pm$ 0.1	770 $\pm$ 1
10^6	10.5 $\pm$ 0.1	3,170 $\pm$ 12
$2.5 \cdot 10^6$	10.7 $\pm$ 0.3	3,090 $\pm$ 100

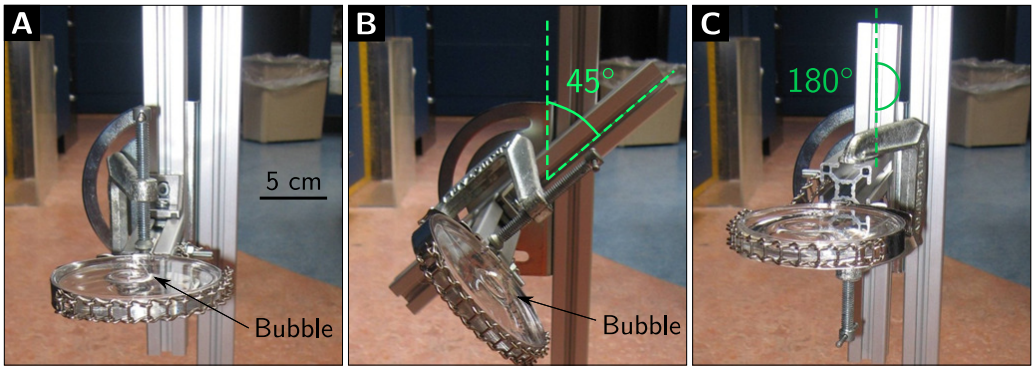

Figure S1: The experimental setup used to rotate the viscous liquid bath. **(A)** Once the air is injected into the petri dish, the upright position of the dish allows gravity to shape the bubble. **(B)** The stage can be rotated within seconds such that the silicone oil does not flow out of the dish, owing to its very high viscosity. **(C)** The dish can thus be rotated 180° with the bubble upside down before puncture.

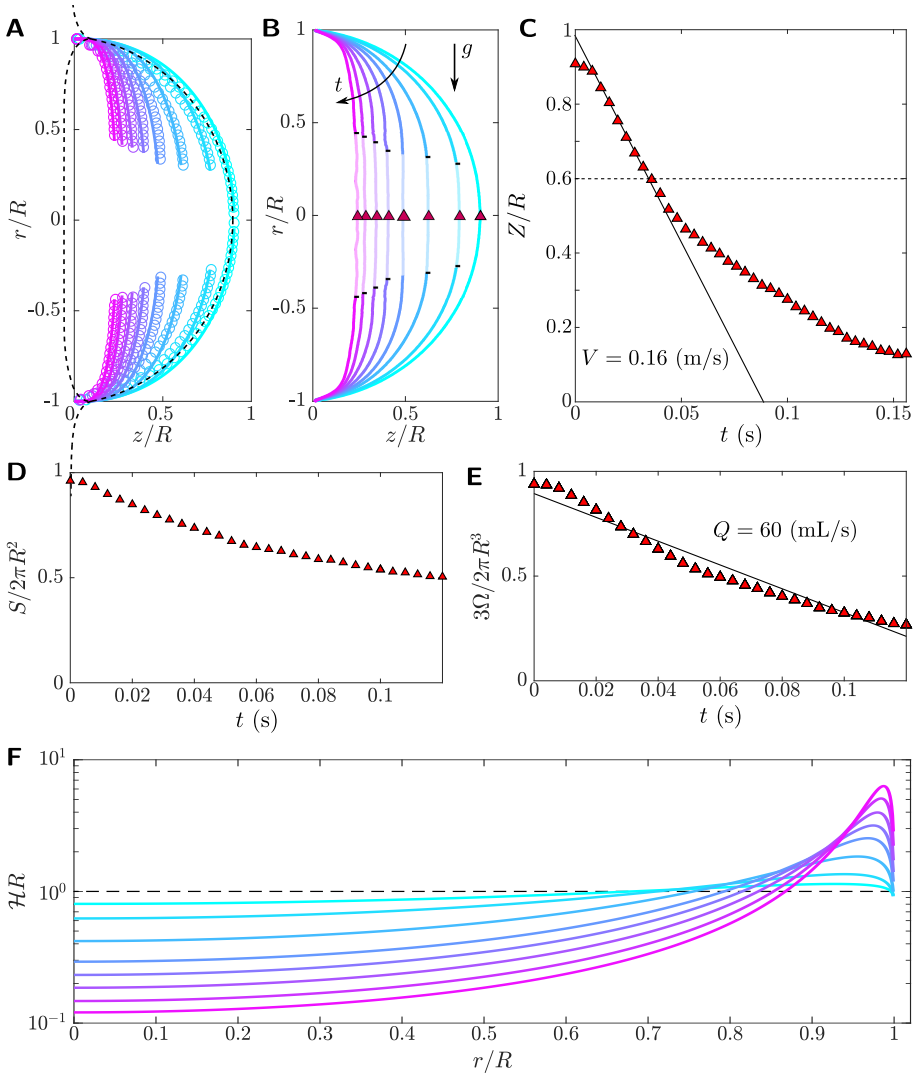

Figure S2: Collapse of a bubble with radius $R = 1.8$ cm. **(A)** Experimental bubble shape (circles) as it collapses and the associated empirical fits (solid lines). The theoretical shape of a bubble with Bond Number Bo = 100 is overlaid on top (dashed line). **(B)** The shape of the collapsing bubble, oriented on its side, plotted in spatial coordinates (r, z), for various times t. The triangles at the apex of the bubble indicate the height $Z(t)$, while the dots on the experimental shapes indicate the position of the growing hole. **(C)** The measured bubble height $Z(t)$ plotted against time, is used to extract the collapse velocity V. **(D)** The surface area of the bubble S decreases with time. **(E)** The volume of the air trapped inside the bubble also decreases with time, yielding a flow rate of air of approximately $Q = 60$ mL/s. **(F)** Scaling the mean curvature $\mathcal{H}$ by the radius of the bubble R, illustrates that the curvature increases locally near the edge of the bubble.

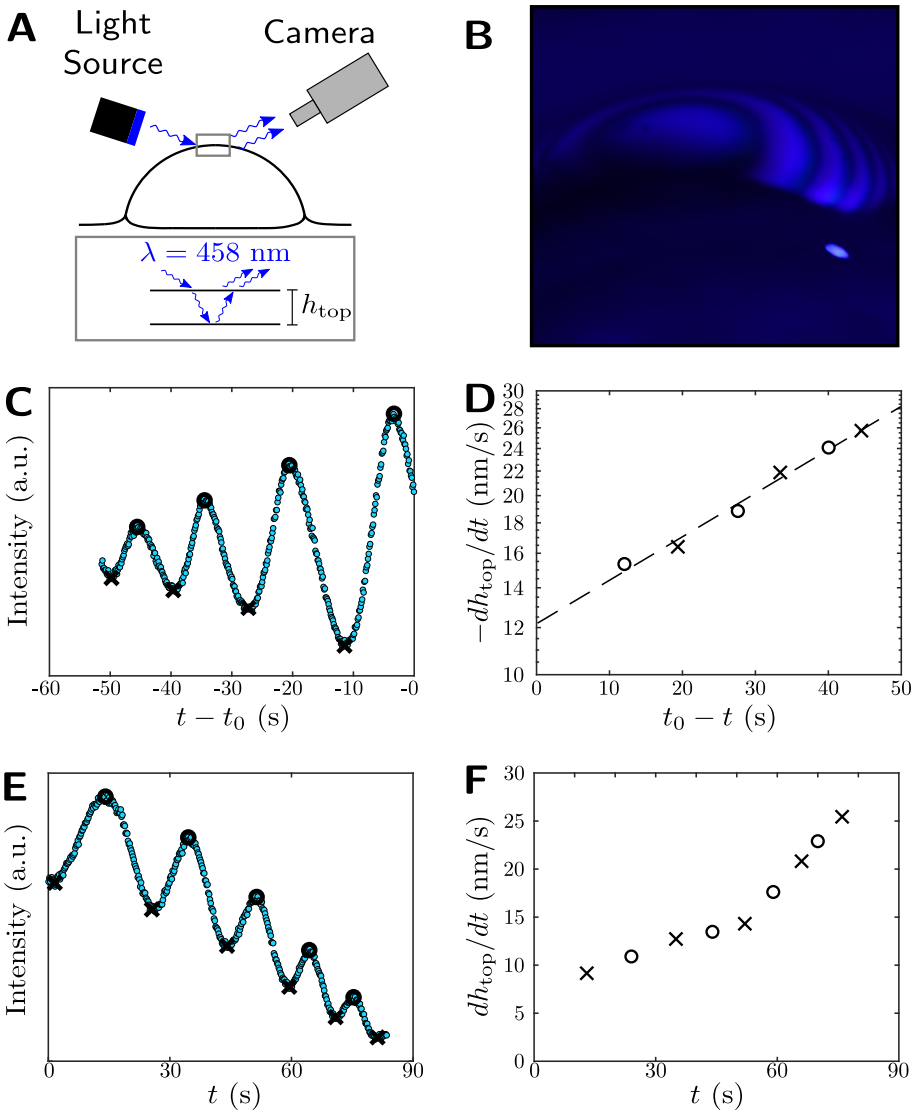

Figure S3: Computing film thickness using interferometry. **(A)** Schematic of the interferometry setup used to estimate the film thickness at the bubble apex h_0. Blue light with wavelength λ = 458 nm is emitted from a light source and its reflection from the bubble cap is recorded by a camera. **(B)** Experimental image highlighting the fringes propagating from the bubble's apex. **(C)** The intensity extracted by the propagating fringes can be plotted against reverse time $t - t_0$, where t_0 is the time of rupture. **D** The peaks (circles) and valleys of the intensity can be used to determine the thinning rate dh_0/dt. **(E)** When the bubble is turned upside-down, the process is reversed and the fringes start propagating towards the apex. **(F)** Upside-down, the film thickness grows at approximately the same speed that it drains, initially on the order of 10 nanometers per second.

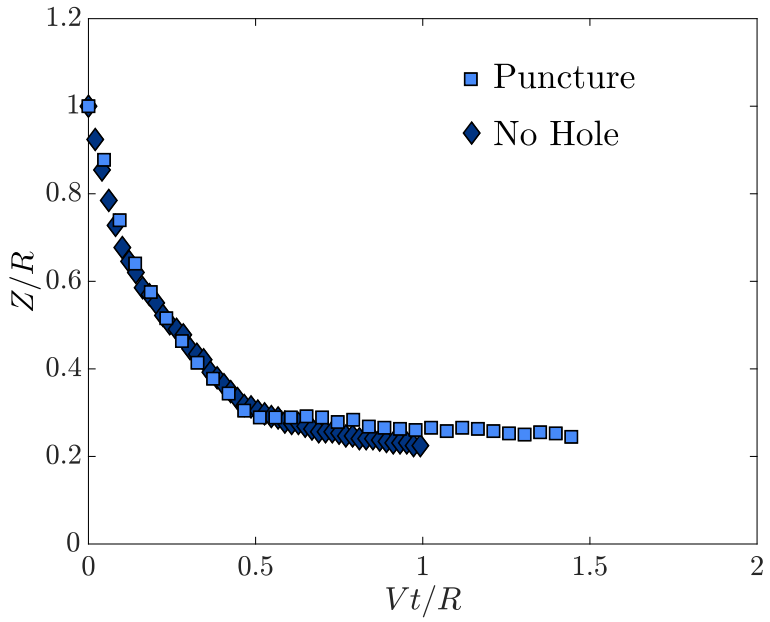

Figure S4: Scaled bubble heights Z/R for experiments involving puncture and evacuation fall onto the same curve when plotted against dimensionless time Vt/R.

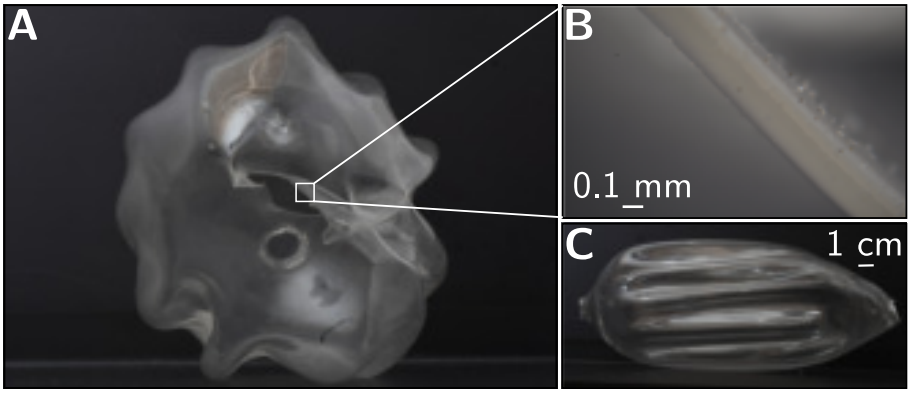

Figure S5: Wrinkling of a molten glass structure. **(A)** Front view of the solidified blown glass. **(B)** The thickness of the blown glass is approximately 200 μm. **(C)** The wrinkles extend throughout the length of the structure.

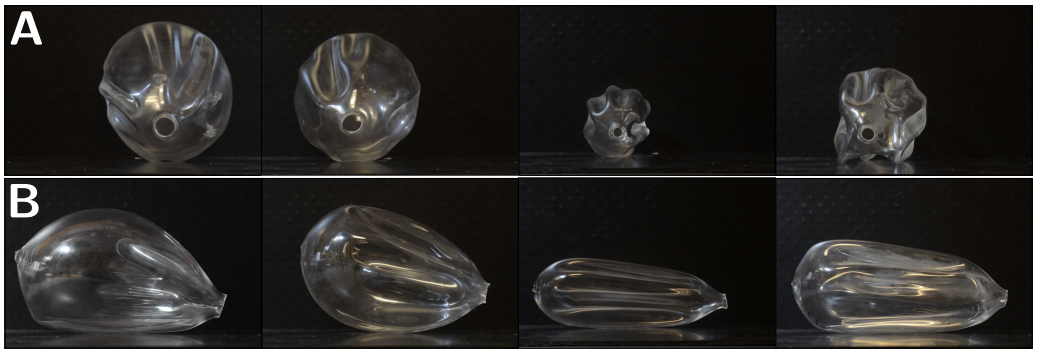

Figure S6: **(A)** Front view of the additional blown glass structures. **(B)** Side view of the additional blown glass structures.

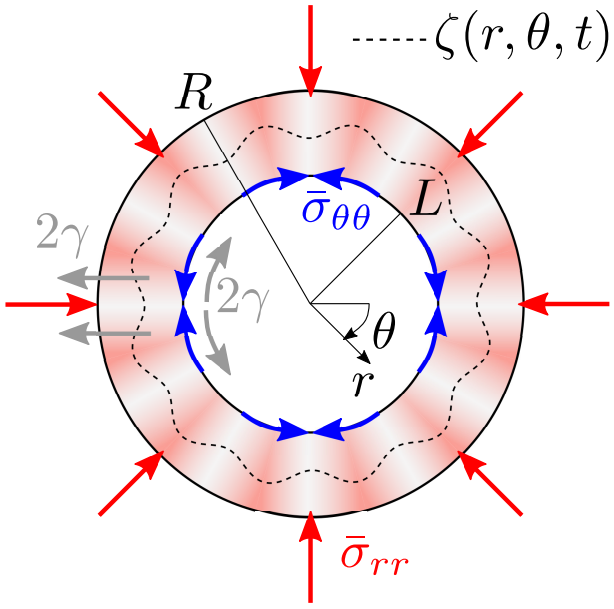

Figure S7: Schematic illustrating the distribution of radial stress $\bar{\sigma}_{rr}$ and azimuthal stress $\bar{\sigma}_{\theta\theta}$ leading to a wrinkled centerline $\zeta(r,\theta,t)$, while being resisted by surface tension γ.

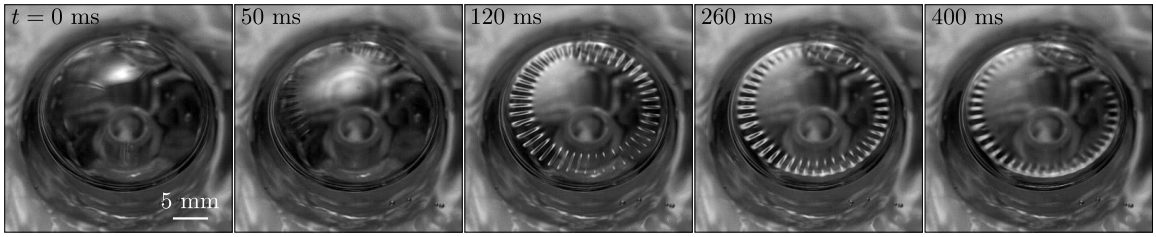

Figure S8: Allowing the air inside the bubble to escape without rupture leads to a wrinkled pattern. Once the bubble has collapsed, the radial extent decreases.

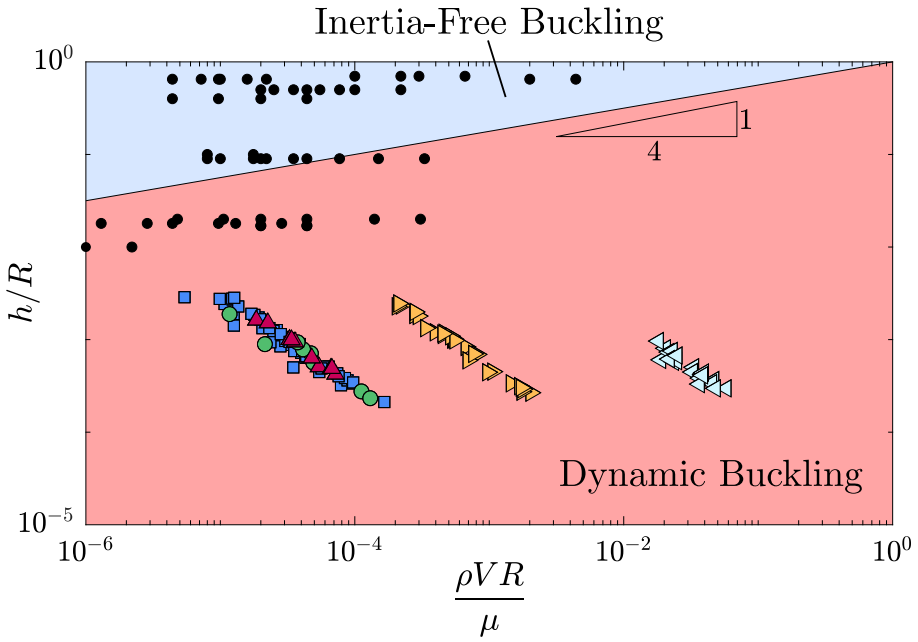

Figure S9: Plotting the aspect ratio h/R against the Reynolds number $\rho VR/\mu$, we observe that the data reported by Le Merrer et al. (*13*) (dark dots) fall fairly consistent within the inertia-free buckling regime, while our data falls (colored symbols) in the dynamic buckling regime.

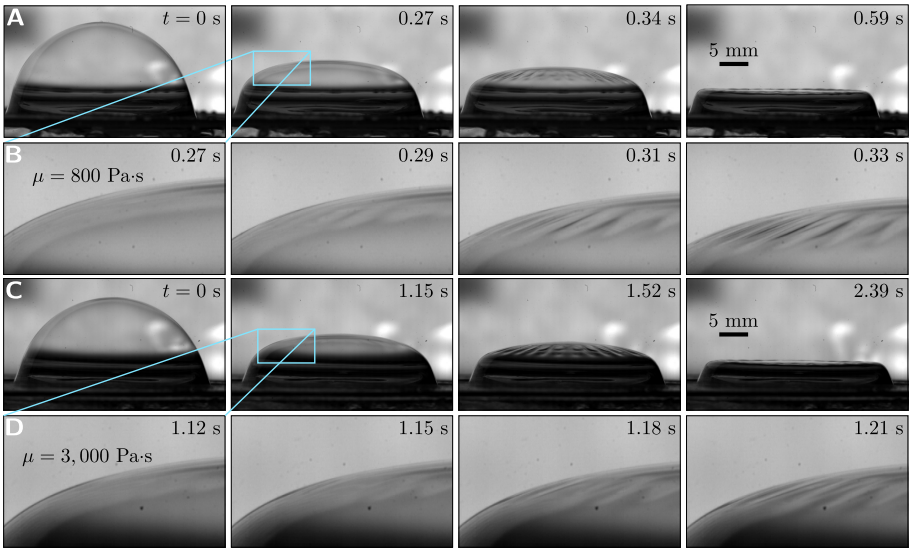

Figure S10: **(A)** Side-view images of the bubble collapse when the viscosity is $\mu = 800$ Pa·s reveals that the collapse occurs within 0.5 s. **(B)** During this collapse, the wrinkles develop over a timescale between 20 and 30 ms. **(C)** At a higher viscosity ($\mu = 3,000$ Pa·s) similar images show that the collapse time increases to 2.3 s. **(D)** Yet the growth of the wrinkles show less dependence on viscosity and continue to develop over a timescale of approximately 30 ms.

Captions for Movies S1 to S8

Movie S1

Collapse of a bubble at the surface of a 1,000 Pa·s silicone oil bath after rupture. The bubble radius is $R = 1$ cm and the total elapsed time is 1.1 seconds. The movie was recorded using a high-speed camera with a frame rate of 200 frames per second.

Movie S2

Collapse of a bubble at the surface of a 1,000 Pa·s silicone oil bath after rupture in an upside down orientation. The bubble radius is $R = 1.8$ cm and the total elapsed time is 0.4 seconds. The movie was recorded using a high-speed camera with a frame rate of 250 frames per second.

Movie S3

Collapse of a bubble at the surface of a 1,000 Pa·s silicone oil bath after rupture in a sideways orientation. The bubble radius is $R = 1.8$ cm and the total elapsed time is 0.5 seconds. The movie was recorded using a high-speed camera with a frame rate of 250 frames per second.

Movie S4

Collapse of a bubble at the surface of a 1,000 Pa·s silicone oil bath without rupture. The bubble radius is $R = 1.2$ cm and the total elapsed time is 0.7 seconds. The movie was recorded using a high-speed camera with a frame rate of 100 frames per second.

Movie S5

Top view of the wrinkling instability for a bubble film with viscosity 3,000 Pa·s in the upright configuration. The bubble radius is $R = 1.5$ cm and the total elapsed time is 2.65 seconds. The movie was recorded using a high-speed camera with a frame rate of 125 frames per second.

Movie S6

Top view of the wrinkling instability for a very thin bubble film with viscosity 3,000 Pa·s in the upright configuration. The bubble radius is $R = 1.5$ cm and the total elapsed time is 0.56 seconds. The movie was recorded using a high-speed camera with a frame rate of 250 frames per second.

Movie S7

Top view of the wrinkling instability for a bubble film with viscosity 100 Pa·s in the upright configuration. The bubble radius is $R = 1.5$ cm and the total elapsed time is 0.19 seconds. The movie was recorded using a high-speed camera with a frame rate of 1,000 frames per second.

Movie S8

Top view for a collapsing bubble film with viscosity 10 Pa·s in the upright configuration where no wrinkling occurs. The bubble radius is $R = 1$ cm and the total elapsed time is 0.02 seconds. The movie was recorded using a high-speed camera with a frame rate of 8,000 frames per second.

Descriptions of Experimental Data Files

Data S1: Experimental Interferometry Data

Collapse speed V for bubbles of viscosity $\mu = 100$, 800 and 3000 Pa·s, for varying initial thickness at the bubble's apex h_0 and bubble radius R.

Data S2: Experimental Wrinkling Data

Number of wrinkles n for collapsing bubbles of viscosity $\mu = 100$, 800 and 3000 Pa·s, for varying collapse speed V, bubble radius R and different bubble orientations.

Data S3: Experimental Blown Data

Number of wrinkles n for the blown glass configurations.

References and Notes

1. M. B. Hallett, S. Dewitt, Ironing out the wrinkles of neutrophil phagocytosis. *Trends Cell Biol.* **17**, 209–214 (2007). doi:10.1016/j.tcb.2007.03.002 Medline

2. M. Kücken, A. C. Newell, A model for fingerprint formation. *EPL* **68**, 141–146 (2004). doi:10.1209/epl/i2004-10161-2

3. L. Mahadevan, R. Bendick, H. Liang, Why subduction zones are curved. *Tectonics* **29**, n/a (2010). doi:10.1029/2010TC002720

4. D. P. Holmes, Elasticity and stability of shape-shifting structures. *Curr. Opin. Colloid Interface Sci.* **40**, 118–137 (2019). doi:10.1016/j.cocis.2019.02.008

5. J. Huang, M. Juszkiewicz, W. H. de Jeu, E. Cerda, T. Emrick, N. Menon, T. P. Russell, Capillary wrinkling of floating thin polymer films. *Science* **317**, 650–653 (2007). doi:10.1126/science.1144616 Medline

6. B. Davidovitch, R. D. Schroll, D. Vella, M. Adda-Bedia, E. A. Cerda, Prototypical model for tensional wrinkling in thin sheets. *Proc. Natl. Acad. Sci. U.S.A.* **108**, 18227–18232 (2011). doi:10.1073/pnas.1108553108 Medline

7. D. Vella, A. Ajdari, A. Vaziri, A. Boudaoud, Wrinkling of pressurized elastic shells. *Phys. Rev. Lett.* **107**, 174301 (2011). doi:10.1103/PhysRevLett.107.174301 Medline

8. D. Vella, J. Huang, N. Menon, T. P. Russell, B. Davidovitch, Indentation of ultrathin elastic films and the emergence of asymptotic isometry. *Phys. Rev. Lett.* **114**, 014301 (2015). doi:10.1103/PhysRevLett.114.014301 Medline

9. H. King, R. D. Schroll, B. Davidovitch, N. Menon, Elastic sheet on a liquid drop reveals wrinkling and crumpling as distinct symmetry-breaking instabilities. *Proc. Natl. Acad. Sci. U.S.A.* **109**, 9716–9720 (2012). doi:10.1073/pnas.1201201109 Medline

10. J. Hure, B. Roman, J. Bico, Stamping and wrinkling of elastic plates. *Phys. Rev. Lett.* **109**, 054302 (2012). doi:10.1103/PhysRevLett.109.054302 Medline

11. G. I. Taylor, in *Proceedings of the Twelfth International Congress of Applied Mechanics, Stanford, 1968* (Springer, 1969), pp. 382–388.

12. J. Teichman, L. Mahadevan, The viscous catenary. *J. Fluid Mech.* **478**, 71–80 (2003). doi:10.1017/S0022112002003038

13. M. Le Merrer, D. Quéré, C. Clanet, Buckling of viscous filaments of a fluid under compression stresses. *Phys. Rev. Lett.* **109**, 064502 (2012). doi:10.1103/PhysRevLett.109.064502 Medline

14. M. Kadoura, N. Saranjam, S. Chandra, H. Fan, Nucleation of bubbles during drying of sprayed paint films. *Prog. Org. Coat.* **99**, 452–462 (2016). doi:10.1016/j.porgcoat.2016.07.002

15. R. Pokorny, Z. J. Hilliard, D. R. Dixon, M. J. Schweiger, D. P. Guillen, A. A. Kruger, P. Hrma, One-dimensional cold cap model for melters with bubblers. *J. Am. Ceram. Soc.* **98**, 3112–3118 (2015). doi:10.1111/jace.13775

16. H. M. Gonnermann, M. Manga, The fluid mechanics inside a volcano. *Annu. Rev. Fluid Mech.* **39**, 321–356 (2007). doi:10.1146/annurev.fluid.39.050905.110207

17. G. Debrégeas, P.-G. de Gennes, F. Brochart-Wyart, The life and death of "bare" viscous bubbles. *Science* **279**, 1704–1707 (1998). doi:10.1126/science.279.5357.1704 Medline

18. R. da Silveira, S. Chaıeb, L. Mahadevan, Rippling instability of a collapsing bubble. *Science* **287**, 1468–1471 (2000). doi:10.1126/science.287.5457.1468 Medline

19. Y. Toba, Drop production by bursting of air bubbles on the sea surface. (II) Theoretical study on the shape of floating bubbles. *J. Oceanogr. Soc. Jpn* **15**, 121–130 (1959). doi:10.5928/kaiyou1942.15.121

20. F. Culick, Comments on a ruptured soap film. *J. Appl. Phys.* **31**, 1128–1129 (1960). doi:10.1063/1.1735765

21. G. Debrégeas, P. Martin, F. Brochard-Wyart, Viscous bursting of suspended films. *Phys. Rev. Lett.* **75**, 3886–3889 (1995). doi:10.1103/PhysRevLett.75.3886 Medline

22. N. Savva, J. W. M. Bush, Viscous sheet retraction. *J. Fluid Mech.* **626**, 211–240 (2009). doi:10.1017/S0022112009005795

23. See the supplementary materials.

24. N. M. Ribe, A general theory for the dynamics of thin viscous sheets. *J. Fluid Mech.* **457**, 255–283 (2002). doi:10.1017/S0022112001007649

25. F. T. Trouton, On the coefficient of viscous traction and its relation to that of viscosity. *Proc. R. Soc. Lond., A Contain. Pap. Math. Phys. Character* **77**, 426–440 (1906). doi:10.1098/rspa.1906.0038

26. P. D. Howell, Models for thin viscous sheets. *Eur. J. Appl. Math.* **7**, 321–343 (1996). doi:10.1017/S0956792500002400

27. S. Bhattacharya, R. V. Craster, M. R. Flynn, Buckling of a thin, viscous film in an axisymmetric geometry. *Phys. Fluids* **25**, 043102 (2013). doi:10.1063/1.4798825

28. G. R. Johnson, L. Morawska, The mechanism of breath aerosol formation. *J. Aerosol Med. Pulm. Drug Deliv.* **22**, 229–237 (2009). doi:10.1089/jamp.2008.0720 Medline

29. J. B. Grotberg, Respiratory fluid mechanics. *Phys. Fluids* **23**, 21301 (2011). doi:10.1063/1.3517737 Medline

30. B. Van De Fliert, P. D. Howell, J. Ockenden, Pressure-driven flow of a thin viscous sheet. *J. Fluid Mech.* **292**, 359–376 (1995). doi:10.1017/S002211209500156X

31. A. Fluegel, Glass viscosity calculation based on a global statistical modelling approach. *Eur. J. Glass Sci. Technol. A* **48**, 13–30 (2007).

32. W. Pietenpol, Surface tension of molten glass. *Physics* **7**, 26–31 (1936). doi:10.1063/1.1745341

33. D. Kumar, T. P. Russell, B. Davidovitch, N. Menon, Stresses in thin sheets at fluid interfaces. *Nat. Mater.* **19**, 690–693 (2020). doi:10.1038/s41563-020-0640-9 Medline

34. J. R. Gladden, N. Z. Handzy, A. Belmonte, E. Villermaux, Dynamic buckling and fragmentation in brittle rods. *Phys. Rev. Lett.* **94**, 035503 (2005). doi:10.1103/PhysRevLett.94.035503 Medline

35. R. Vermorel, N. Vandenberghe, E. Villermaux, Rubber band recoil. *Proc. R. Soc. A* **463**, 641–658 (2007). doi:10.1098/rspa.2006.1781

36. R. Vermorel, N. Vandenberghe, E. Villermaux, Impacts on thin elastic sheets. *Proc. R. Soc. A* **465**, 823–842 (2009). doi:10.1098/rspa.2008.0297

37. F. Box, O. Kodio, D. O'Kiely, V. Cantelli, A. Goriely, D. Vella, Dynamic buckling of an elastic ring in a soap film. *Phys. Rev. Lett.* **124**, 198003 (2020). doi:10.1103/PhysRevLett.124.198003 Medline